ESI Preprints **Not Peer-reviewed**

Conditional Thermomechanical Feasibility of a Bimetal Actuated Thermal Capsule

Nguyen Thanh Duong
Institute of Technology, Ha Noi, Vietnam

Approved: 09 November 2026
Posted: 11 November 2026

Copyright 2026 Author(s)
Under Creative Commons CC-BY 4.0
OPEN ACCESS

Cite As:
Nguyen, T.D. (2026). *Conditional Thermomechanical Feasibility of a Bimetal Actuated Thermal Capsule.* ESI Preprints. https://doi.org/10.19044/esipreprint.11.2026.p78

Abstract

A miniature thermal capsule must cool rapidly into a narrow temperature band while suppressing heat loss after contact release. This study couples geometry-dependent actuator stiffness, unilateral contact and pressure-dependent gap transfer to a two-node enthalpy model. A massless intermediate node enforces heat-flux continuity between the joint and its downstream resistance. A grid of 10,800 configurations tests entry into −21 to −19 °C within 3 s and uninterrupted residence for at least 30 s, together with provisional displacement and force requirements. At 1, 10 and 100 Pa, respectively, 148, 68 and 0 of 3600 configurations pass at nominal inputs. No nominally feasible candidate passed all 16 tested tolerance corners. Nominal residence at 1 and 10 Pa is right-censored, with lower bounds of 30.253 and 30.254 s, respectively; at 100 Pa the observed residence is 7.333 s. These results assume an external resistance of 22.80 K W^{-1} and a gap regularization length of 1 μm. Illustrative metal sections explain only 1.03% of that resistance, making the counts conditional on an unidentified assembly and boundary network. Removing phase excess leaves the nominal zero-gas response unchanged, indicating isolation-dominated residence in that scenario. The contribution is a quantified loss of feasibility at tested tolerance corners, not experimental performance or an exclusion of all continuous designs.

Keywords: Thermostatic bimetal, unilateral contact, gas conduction, thermal isolation, design feasibility

Introduction

Passive thermal switches regulate heat flow by changing contact or geometry. Differential expansion, contact-based actuation and magnetic mechanisms have been demonstrated in several assemblies (Castelli, Garg, Zhu, Sashital, Shimokusu, and Wehmeyer, 2023; Guo, Zhang, Huang, Hu, and Liu, 2017; Kommandur and Kishore, 2023; Park, Li, and Weisensee, 2024; Xiao, Kishore, and Booten, 2025). Their performance does not establish the response of a miniature capsule: contact load, surface condition, residual gas and fixed thermal paths jointly determine the assembled conductance (Cooper, Mikic, and Yovanovich, 1969). Bistable origami offers another route to large switching ratios (Tan, Lyu, Yang, Xu, Qiao, Song, Yang, and Liu, 2026). A large free stroke can coexist with inadequate loading or excessive heat leakage after release.

The scientific problem is whether one set of bimetal dimensions and assembly interference can satisfy two competing thermal requirements: rapid entry into −21 to −19 °C and at least 30 s of uninterrupted residence. Strong initial thermal coupling favors rapid cooling, whereas persistent coupling after unloading drives the surface below the band. Geometric deviations alter both stiffness and the temperature of contact release, so a nominally passing trajectory may have little tolerance margin.

Phase-change material introduces a second ambiguity. Its latent capacity helps only when cooling enthalpy release overlaps the operating state (Bianco, De Rosa, and Vafai, 2022; Farid, Khudhair, Razack, and Al-Hallaj, 2004; Righetti, Zilio, Doretti, Longo, and Mancin, 2021; Zalba, Marín, Cabeza, and Mehling, 2003). The published SP-21 freezing interval extends below the target band (Rubitherm Technologies GmbH, 2022), and encapsulated materials can behave differently during heating and cooling (Heinz and Moser, 2023). Residence therefore cannot be attributed to latent heat merely because PCM is present.

The method integrates a signed-gap contact closure, geometry-dependent stiffness, pressure-dependent gas conduction and a two-node enthalpy balance. These established physical ingredients are combined into a joint mechanical–thermal feasibility test; no new universal contact law is claimed. Geometry grids and tolerance-corner calculations quantify where displacement, loading and timing requirements cease to overlap. Separate resistance and regularization sensitivities identify which exclusions depend on unmeasured inputs.

The study answers whether the sampled capsule retains a feasible region under declared geometric deviations, and what controls the loss of that region. It is a conditional numerical design study. Its principal result is the absence of an all-corner passing candidate at the reference network, rather than qualification of one favorable nominal design.

Methods

Capsule and operating requirement

The capsule has a 10.40 mm outside diameter, a 10.00 mm active diameter and a 2.10 mm axial envelope (Figure 1). A 0.10 mm lid covers a 1.65 mm cavity containing 0.15 mm headspace, 1.10 mm upper SP-21, a 0.15 mm copper spreader and 0.25 mm lower SP-21. Below this cavity are a 0.05 mm diaphragm, a 0.25 mm dry actuator chamber and a 0.05 mm bottom retainer. The retainer lies outside the dry chamber but inside the total height. The external copper load disk is excluded from this envelope.

Both thermal nodes start at 25 °C and the cold boundary is −196 °C. The copper node must enter −21 to −19 °C by 3 s and remain continuously within that interval for at least 30 s. A 33 s observation horizon is sufficient to establish that requirement for timely entry. The node represents a uniform face temperature; spatial uniformity is not established.

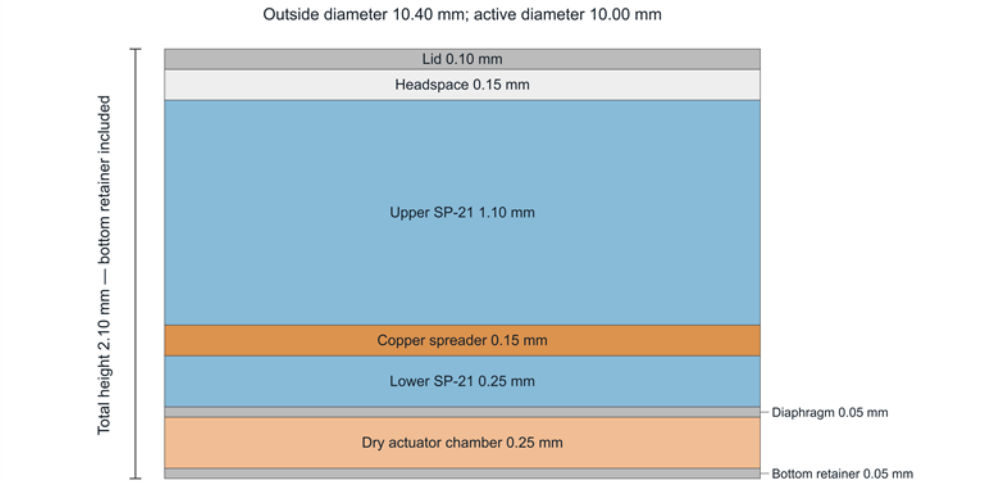


Figure 1: Capsule cross-section

Geometry and thermal inventory

The thermal inventory is derived from the axial stack and the active circular area. The total height H_{tot} combines lid thickness t_{lid}, cavity height h_{cav}, diaphragm thickness t_{dia}, dry-chamber height h_{dry} and retainer thickness t_{ret}:

$$H_{tot} = t_{lid} + h_{cav} + t_{dia} + h_{dry} + t_{ret} = 0.10 + 1.65 + 0.05 + 0.25 + 0.05 = 2.10\,mm \quad (1)$$

For active diameter D_d, the disk area A_d determines PCM volume V_{PCM} from the upper and lower layer thicknesses, t_{upper} and t_{lower}. With assumed density ρ_{PCM}, the fill mass is m_{PCM}; A_c denotes the separate contact-pad area:

$$A_d = \frac{\pi {D_d}^2}{4}, \quad V_{PCM} = A_d(t_{upper} + t_{lower}) \\ m_{PCM} = \rho_{PCM} V_{PCM}, \quad A_c = 20\, mm^2 \tag{2}$$

Table 1 separates copper-node capacity C_c, bulk sensible capacity C_s and phase excess Q_{ph}. PCM mass assumes 1300 kg m^{-3}; the supplier lists a lower liquid density (Rubitherm Technologies GmbH, 2022). C_c includes the 0.85-coverage spreader and the external 10 mm diameter, 0.50 mm thick load disk. Enclosure capacity includes the lid, diaphragm and retainer, plus an annular wall between diameters 10.10 and 10.40 mm. Its height is 2.10 − 0.10 − 0.05 = 1.95 mm, spanning the cavity, diaphragm and dry chamber between end plates. Density and specific heat are 8000 kg m^{-3} and 500 J kg^{-1} K^{-1}. Flanges, welds, actuator and sensor capacities are omitted.

Table 1: Thermal inventory

Quantity	Model value
PCM mass	0.138 g
Copper-node capacity C_c	0.170 J K^{-1}
Enclosure capacity	0.101 J K^{-1}
Bulk sensible capacity C_s	0.376 J K^{-1}
Phase excess Q_{ph}	26.88 J
Freezing interval	−24 to −21 °C
Internal conductance G_{int}	0.343 W K^{-1}
Reference resistance R_s	22.80 K W^{-1}
Reference bypass G_b	0 W K^{-1}

Internal conduction combines parallel half-thickness PCM paths at 0.60 W m^{-1} K^{-1} (Rubitherm Technologies GmbH, 2022) with a 5 µm Parylene C layer. The coating conductivity is assumed constant at 0.084 W m^{-1} K^{-1} throughout the simulated temperature range, including below 0 °C. This is a modelling input, not a measured cryogenic conductivity curve. The service-temperature discussion in (Specialty Coating Systems, 2022) does not establish temperature-independent conductivity. Coating thickness and conductivity are held fixed in G_{int}; their temperature dependence and interfacial resistance remain unresolved. Table 1 is a reduced thermal inventory, not an assembly measurement.

Coupled thermomechanical model

Displacement and contact force

Figure 2 defines the three-arm IMPHY 108SP actuator, with 0.12 mm arm width and 5.05 mm pad diameter. Free retraction u_f depends on arm length L_a, thickness t_b and specific curvature κ_s (Aperam Alloys Imphy, 2025). Strip bending supplies the relative stiffness scaling (Shivalik Bimetal Controls, n.d.; Timoshenko, 1925) at fixed width, effective modulus and

restraint. Nominal inputs are $L_{a,0}$ = 2 mm, $t_{b,0}$ = 0.10 mm and k_0 = 1800 N m^{-1}. The thermal reduction sets actuator temperature T_a equal to copper temperature T_c, eliminating a separate actuator energy balance:

$$u_f(T_a) = \frac{\kappa_s {L_a}^2}{2t_b}[25 - T_a]_+, \quad T_a = T_c$$
$$k_{eq} = k_0\left(\frac{t_b}{t_{b,0}}\right)^3\left(\frac{L_{a,0}}{L_a}\right)^3 \tag{3}$$

The equality $T_a = T_c$ represents the limit of rapid thermal equilibration with the copper. It requires actuator thermal relaxation to be short relative to the cooling transient and small temperature gradients over the active arms. Neither condition has been measured; small thickness alone does not establish them. Thermal lag or cooling through the supports could shift retraction and release, so this assumption is not known to be conservative.

The value k_0 = 1800 N m^{-1} is an assumed assembly stiffness. An elementary consistency estimate treats three identical straight arms as independent cantilevers with equal end translation: $k_0 = 3(3EI/L_{a,0}^3)$, where $I = w\, t_{b,0}^3/12$ and w = 0.12 mm. The stated dimensions then require E = 160 GPa. This arithmetic makes the reference stiffness compatible with that idealization; it neither identifies the composite modulus nor validates the formed geometry. A rotation-constrained tip changes both mechanical stiffness and thermally induced motion, so one cannot combine its stiffness with the free-tip retraction law without a structural solution. At nominal dimensions, 35 μm interference gives 63 mN. That identity is not a calibration. Unverified U2: effective modulus, pad restraint, arm coupling, residual stress and force–displacement behavior remain unmeasured.

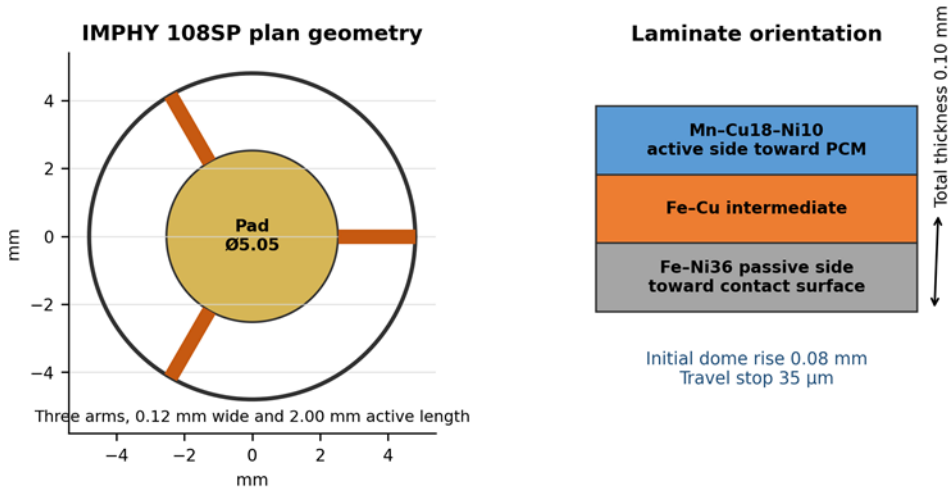


Figure 2: Actuator geometry

With $[x]_+ = \max(x,0)$, signed initial gap $g_0 < 0$ denotes interference $d_0 = -g_0$. Free retraction first consumes elastic compression δ_{el}, reducing force F_c and contact pressure p over area A_c; subsequent motion opens gap g:

$$\begin{gathered} \delta_{el} = [-g_0 - u_f]_+, \quad F_c = k_{eq}\delta_{el}, \quad p = \frac{F_c}{A_c} \\ g = min([g_0 + u_f]_+, s_{max}), \quad s_{max} = 35\,\mu m \\ T_{rel} = 25 - \frac{2t_b d_0}{\kappa_s {L_a}^2} \end{gathered} \tag{4}$$

Here s_{max} = 35 μm is the separation stop and T_{rel} is the zero-force release temperature. The closure separates free motion from actual compression; it omits snap-through, residual stress and arm coupling.

Contact and gap conductance

Joint conductance G_j combines solid-contact, gas and radiation branches between the hot and cold joint faces, $T_{j,h}$ and $T_{j,c}$. The hot face is approximated by T_c; the cold face is solved from the downstream heat balance in Eq. (6). Mechanical pressure $p = F_c/A_c$ enters the surrogate contact law (Cooper, Mikic, and Yovanovich, 1969), while chamber pressure p_g controls the gas mean free path λ (COMSOL AB, n.d.):

$$\begin{gathered} G_j = A_c\, h*\, (p/p*)^n + A_c\, k_{g,eff}/Y + G_{rad} \\ k_{g,eff} = k\infty\, Y/(Y + \zeta\lambda), \quad Y = g + g_r \\ \lambda = k_B\, T_{g,K}/(\sqrt{2}\,\pi\, {d_m}^2\, p_g), \quad \zeta = 2\beta(2-\alpha)/\alpha \\ T_{g,K} = (T_{j,h,K} + T_{j,c,K})/2 \\ G_{rad} = \varepsilon_{eff}\,\sigma\, A_c\, (T_{j,h,K} + T_{j,c,K}) \\ \times\, ({T_{j,h,K}}^2 + {T_{j,c,K}}^2) \end{gathered} \tag{5}$$

In Eq. (5), h* is reference contact conductance per unit area, p* its pressure normalization and n the exponent. Their assumed values are 90,000 W m^{-2} K^{-1}, 3151.98 Pa and 0.95, with A_c = 20 mm². The model is not a calibrated rough-contact law because asperity slope, roughness and hardness are unavailable.

Unverified U3: the magnitude h* and exponent n are scenario inputs, not values furnished by Cooper, Mikic, and Yovanovich (1969). The cited contact theory motivates pressure dependence but requires surface information absent here. The reference initial pressure is approximately 3.15 kPa and the solid branch conductance is approximately 1.80 W K^{-1}; its inverse is a joint resistance and is not included again in Rs. At 1 Pa, multiplying h* by 0.25 or 4 gives entry times of 4.322 or 2.249 s, respectively; these are deterministic scenarios without assigned probabilities.

Here $k_{g,eff}$ is effective gas conductivity, k∞ its continuum input and $Y = g + g_r$ the regularized separation. The gas mean $T_{g,K}$ uses the two joint-face temperatures in kelvin. An air-like reference gas is represented by assumed

molecular diameter d_m = 0.37 nm and the air jump coefficient β = 1.7 (COMSOL AB, n.d.). The constant k∞ = 0.010 W m^{-1} K^{-1} is a prescribed scenario value, not a validated air-property correlation across the simulated temperatures. Effective accommodation α = 0.8 is assumed for both faces; it is not measured for the actual gas–surface pair. These constants determine λ and ζ with Boltzmann constant k_B. Other inputs are g_r = 1 μm and ε_{eff} = 0.10; σ is the Stefan–Boltzmann constant. Chamber pressure is prescribed, and p_g = 0 gives zero gas transfer. Actual gas composition, condensation and pressure evolution are unresolved; the cold bath does not imply nitrogen in the chamber.

When ζλ dominates Y, rarefaction suppresses gas transfer. Near contact, g_r prevents a singularity but is not a measured clearance. Solid bridges and nonuniform gas-filled area can invalidate the full-area closure. Sensitivity to g_r therefore measures dependence on a modelling assumption, not the accuracy of nanoscale contact physics.

Unverified U4: pressure and gas properties are prescribed inputs rather than measured chamber conditions. A new 27-case cross-product sensitivity combines k∞ = 0.005, 0.010 and 0.020 W m^{-1} K^{-1} with α = 0.5, 0.8 and 1.0 at 1, 10 and 100 Pa, using the corrected junction temperature in every case. These deliberately broad alternatives test dependence on the closure; they do not constitute a validated uncertainty distribution.

External resistance and boundary condition

The joint is followed by series resistance R_s connecting its cold face $T_{j,c}$ to the bath T_b. A massless intermediate node imposes equal heat rates through the joint and R_s at every integration stage. The hot face is set to $T_{j,h}$ = T_c, neglecting upstream spreading resistance; the entire declared R_s is downstream. Bypass conductance G_b connects copper directly to the bath. Joint heat rate Q_j and total outgoing heat rate Q_{out} satisfy

$$\begin{aligned} Q_j &= G_j(T_{j,h} - T_{j,c}) = (T_{j,c} - T_b)/R_s \\ Q_{out} &= Q_j + G_b(T_c - T_b),\ T_{j,h} = T_c \\ R_s &= R_{Cu} + R_{316L} + R_u + R_{bnd} \\ R_i &= \ell_i/(k_i\, A_i),\ R_{bnd} = 1/(h_b\, A_b) \end{aligned} \tag{6}$$

Table 2: External resistance inventory

Contribution	Reference estimate
0.50 mm copper, k = 400 W m^{-1} K^{-1}	0.0625 K W^{-1}
0.05 mm 316L, k = 14.6 W m^{-1} K^{-1}	0.1712 K W^{-1}
Unassigned reference remainder	22.56 K W^{-1}

In the resistance decomposition, R_i = ℓ_i/(kiAi) describes a section of length ℓ_i, conductivity k_i and area A_i. R_{Cu} and R_{316L} are the two metal terms in

Table 2; R_u groups unresolved spreading and interfaces. Boundary resistance R_{bnd} uses heat-transfer coefficient h_b and bath-exposed area A_b.

Both metal estimates use the 20 mm² contact area. Their sum is 0.2337 K W⁻¹, only 1.03% of the reference R_s. These are conditional one-dimensional sections, not proof that the manufactured heat path contains them in series. R_u represents unresolved spreading, mounting and interfaces. A wall path that bypasses the joint belongs in G_b; a coating already included in another branch must not be counted twice.

The reference value R_s = 22.795485615 K W⁻¹ (displayed as 22.80 K W⁻¹) is retained solely to reproduce the submitted model. Its physical decomposition has not been identified. After the illustrative metal terms, 22.5618 K W⁻¹ remains for $R_u + R_{bnd}$. If that entire remainder were attributed to a bath boundary over the 10 mm disk area, it would require h_b = 564.3 W m⁻² K⁻¹. This is an inverse calculation, not a measured boiling coefficient. A positive R_u permits many other decompositions. Unverified U1: the wetted area, bath heat-transfer regime, mounting and interface resistances, and intermediate thermal storage are unknown; therefore 22.80 K W⁻¹ is not a validated assembly property.

The scalar junction balance is solved within $T_b \le T_{j,c} \le T_c$. At the initial nominal state and 1 Pa, $T_{j,c}$ = 19.739 °C despite T_b = −196 °C: substituting the bath into the gas and radiation laws would therefore misrepresent the joint temperature drop. The revised closure conserves series heat flow but neglects intermediate thermal storage and spatial face gradients. It remains a reduced network, not a resolved assembly model.

Uncertainty is treated as scenario sensitivity because component uncertainty estimates and covariances are unavailable. If those data were known, first-order propagation would use $u^2(Rs) = (\nabla Rs)^T\, Cx\, (\nabla Rs)$ for the component-input covariance matrix Cx; the unknown remainder prevents assigning a defensible numerical standard uncertainty here. The new resistance sweep spans 0.5–2 times the reference at each tested pressure. These factors are not a confidence interval, and changing Rs alone does not resolve uncertainty in network topology or bypass leakage.

Cooling enthalpy and energy balance

The second node represents bulk temperature T_p and enthalpy H_p, including PCM and enclosure sensible capacity C_s. The supplier gives 285 kJ kg⁻¹ combined storage over −30 to 15 °C (Rubitherm Technologies GmbH, 2022). Subtracting a 2 kJ kg⁻¹ K⁻¹ sensible baseline gives a planning phase excess of 195 kJ kg⁻¹, or Q_{ph} = 26.88 J for the assumed fill. The dimensionless phase function $f(T_p)$ varies between zero and one over the freezing bounds T_s = −24 °C and T_l = −21 °C:

$$H_p(T_p) = C_s T_p + Q_{ph} f(T_p)$$
$$f(T) = min(1, max(0, \frac{T - T_s}{T_l - T_s})), \quad T_s = -24\,°C, T_l = -21\,°C \tag{7}$$

Equation (7) is monotone, allowing T_p to be recovered from H_p at each time step. Internal conductance G_{int} transfers heat between the bulk and copper nodes, whose heat capacity is C_c. With time t, the coupled balances are a two-node reduction of enthalpy-based modelling (Voller, Cross, and Markatos, 1987; Voller and Prakash, 1987):

$$C_c \frac{dT_c}{dt} = G_{int}(T_p - T_c) - Q_{out}$$
$$\frac{dH_p}{dt} = -G_{int}(T_p - T_c) \tag{8}$$

$$T_c(0) = T_p(0) = 25\,°C, \quad T_b = -196\,°C, \quad t_f = 33\,s \tag{9}$$

Here t_f = 33 s is the observation horizon and T_b is the prescribed cold boundary. Internal exchange appears with opposite signs in Eq. (8), conserving energy between nodes. Finite thermal lag allows T_c to reach the target while T_p remains above the freezing interval; residence can therefore arise from isolation and sensible storage without latent release.

Unverified U5: Q_{ph} is a planning excess, not a measured capsule-scale cooling enthalpy. The supplier's solid and liquid densities are approximately 1300 and 1200 kg m^{-3}, respectively; the code retains the solid-density-based mass of 0.138 g to reproduce the reference calculation. Filling the same nominal volume at the stated liquid density would instead give approximately 0.127 g, so the actual fill mass must be measured. The supplier's 50 mL minimum encapsulation volume is about 472 times the nominal 0.106 mL PCM volume (Rubitherm Technologies GmbH, 2022). Supercooling, nucleation, phase segregation and compatibility with the enclosure therefore remain unresolved. Scaling phase excess while retaining sensible capacity is a numerical isolation test, not qualification of SP-21 in this capsule.

Entry residence and feasibility

To compare geometries consistently, the response is reduced to event-based quantities rather than final temperature alone. Entry time t_{entry} is the first arrival in the closed target band; t_{exit} is the first later departure through either boundary. True residence τ and observed residence τ_{obs} over 33 s are then

$$t_{entry} = inf\{t \geq 0 : -21 \leq T_c(t) \leq -19\}$$
$$t_{exit} = inf\{t > t_{entry} : T_c(t) < -21 \; or \; T_c(t) > -19\}$$
$$\tau = t_{exit} - t_{entry}; \quad \tau_{obs} = min(t_{exit}, 33\,s) - t_{entry} \tag{10}$$
$$t_{exit} > 33\,s : \tau \geq \tau_{obs}; \quad t_{exit} \leq 33\,s : \tau = \tau_{obs}$$

If no exit occurs by 33 s, only the lower bound $\tau \geq \tau_{obs}$ is known. The symbol ≥ in the tables denotes right censoring, not a confidence interval. No-entry cases have undefined residence and entry force and fail the timing test.

All trajectories start at 25 °C, so continuity places first entry at T_c = −19 °C even if later evolution is nonmonotonic. Force is evaluated at that interpolated state. The mechanical gates define allowable travel and loading; Ω is the set of design vectors θ = (L_a, t_b, κ_s, d_0) meeting these gates and the timing limits:

$$30\ \mu m \ \leq\ u_f\ (-19.90\ ^\circ C)\ \leq\ 40\ \mu m$$
$$20\ mN\ \leq\ F_c(0)\ \leq\ 100\ mN,\quad F_c(t_{in})\ \geq\ 0.5\ mN \tag{11}$$

$$\theta\ =\ (L_a, t_b, \kappa_s, d_0)$$
$$\Omega\ =\ \{\theta :\ Eq.(11), t_{in}\ \leq\ 3\ s, t_{hold}\ \geq\ 30\ s\} \tag{12}$$

Here $t_{in} = t_{entry}$ and $t_{hold} = \tau_{obs}$. The 30–40 μm free-travel gate at a 44.9 K drop brackets the nominal 35.02 μm prediction; it is distinct from the 35 μm separation stop. The 20–100 mN initial-force window brackets the nominal 63 mN load and corresponds to 1–5 kPa over 20 mm². The 0.5 mN entry minimum (25 Pa) requests a small residual compressive load before release; no force minimum applies afterward. These analyst-selected screening windows provide a common comparison basis. They are neither measured conductance thresholds nor verified strength or manufacturing limits, and the feasible counts depend on them.

A configuration passes only when entry is no later than 3 s and at least 30 uninterrupted seconds are observed. A censored duration below 30 s cannot certify residence; within this protocol it also implies entry after 3 s.

Parameter sampling and numerical verification

The design vector θ contains L_a, t_b, κ_s and d_0. The grid combines nine lengths (1.80–2.20 mm), five thicknesses (0.095–0.105 mm), five curvatures (37.44–40.56 × 10^{-6} K^{-1}) and sixteen interferences (25–40 μm), giving 3600 points per pressure. Curvature spans the supplier ±4% range (Aperam Alloys Imphy, 2025); the other intervals are declared design variations. Alternative arm lengths need a separate ring-fit check.

The exact grid is specified by inclusive uniform sequences: length increment 0.05 mm, thickness increment 0.0025 mm, curvature increment 0.78 × 10^{-6} K^{-1}, and interference increment 1 μm, combined with $p_g \in \{1, 10, 100\}$ Pa. Thus 9 × 5 × 5 × 16 × 3 = 10,800 distinct configurations are evaluated. The 0.095–0.105 mm sampling interval is a declared design range; part of it falls below the supplier's listed 0.10 mm minimum strip thickness and is not a confirmed procurement tolerance.

Fourth-order Runge–Kutta integration uses 0.005 s steps, with 0.0025 s refinement for passing or near-boundary points and 0.00125 s checks for selected cases. Crossings are linearly interpolated. The energy change ΔE,

relative to initial temperature T_0 and enthalpy $H_{p,0}$, is compared with integrated outgoing heat through residual r_E:

$$\Delta E = C_c(T_c - T_0) + H_p - H_{p,0}$$
$$r_E = \frac{|\Delta E + \int_0^t Q_{out}\, d\tau|}{max(\int_0^t Q_{out}\, d\tau, 10^{-12}\, J)} \quad (13)$$

The maximum grid energy residual is 3.20×10^{-14}; shared integration stages make this an algebraic consistency check. For the five nominal pressure cases, halving the step from 0.0025 to 0.00125 s changes entry and residence by at most 2.37×10^{-6} s and copper temperature by 9.10×10^{-7} K on a common 0.05 s output grid. An independent constant-conductance, zero-phase-excess matrix-exponential solution agrees at 33 s within 8.53×10^{-14} K. Its conductance is 0.010 W K^{-1}, with the same capacities and initial state. A separate bisection solution of 2880 static junction cases agrees with Newton iteration within 5.69×10^{-14} K. These reproducible numerical checks do not physically validate the contact law.

A fresh full execution reproduced the 10,800 grid cases, near-boundary refinement, 3,456 tolerance cases and auxiliary calculations. The resulting CSV values were compared against the supplied archive; no classification or numerical discrepancy above the declared comparison tolerance was found. The accompanying junction_grid.csv supplies the 10,800 configuration records; Appendix A of the accompanying response letter specifies the grid ordering and reproduction procedure. Energy residuals test conservation consistency; time-step comparisons and the independent benchmark test numerical behavior, not physical accuracy.

Sensitivity S_x^y is the logarithmic response of output y to input x, normalized by reference values x_0 and y_0. For free displacement $u = u_f$ and blocked-force product $ku = k_{eq}\, u_f$, the scalings are

$$S_x^{\,y} = \frac{\partial\, ln(y/y_0)}{\partial\, ln(x/x_0)}$$
$$(S_{L_a}^{\,u}, S_{t_\beta}^{\,u}, S_{\kappa_s}^{\,u}) = (2, -1, 1) \quad (14)$$
$$(S_{L_a}^{\,ku}, S_{t_\beta}^{\,ku}, S_{\kappa_s}^{\,ku}) = (-1, 2, 1)$$

These derivatives explain geometry trends but do not directly determine unilateral contact force. Each nominally feasible $\theta \in \Omega$ is perturbed by ±1% length, ±2.5% thickness, ±4% curvature and ±1 μm interference. The tested subset requires all 16 corner combinations to pass. Corner failure excludes that candidate under the stated all-corner criterion; this test does not classify every interior tolerance point or prove that response extrema occur at corners:

For each passing nominal candidate, all 2^4 combinations use multiplicative factors {0.99, 1.01} for L_a, {0.975, 1.025} for t_b, {0.96, 1.04} for κ_s, and additive offsets {−1, +1} μm for d_0; chamber pressure is fixed. Corners are integrated at 0.005 s. An independent audit reconstructs every

corner, recalculates its mechanical and timing flags, checks censoring, and recomputes each 16-row summary. No claim is made that all corner trajectories received step-halving verification.

$$\Omega_{corner} = \{\theta \in \Omega : \theta + \Delta\theta \in \Omega \; for \; every \; tested \; corner \; \Delta\theta\} \quad (15)$$

Results

Pressure controls post-release cooling

The pressure comparison holds geometry and the thermal network fixed, so differences isolate the assumed gas-transfer law. Figure 3 shows the copper trajectories and Table 3 separates timely entry from sustained residence.

Table 3: Nominal pressure response

p_g, Pa	Entry, s	Residence, s	T_c(33 s), °C
0 limit	2.746	≥30.253	−19.888
1	2.746	≥30.253	−19.962
10	2.746	≥30.254	−20.693
100	2.738	7.333	−21.901
100,000	2.362	0.277	−62.835

At nominal geometry, increasing pressure from 1 to 100 Pa advances entry by approximately 0.01 s but reduces residence from a lower bound of 30.253 s to 7.333 s. Entry time is therefore a poor indicator of regulation after unloading. Initial solid contact supports rapid cooling; subsequent gas transfer controls whether the copper cools below the target band.

At 10 Pa, T_c(33 s) = −20.693 °C is only 0.307 K above the lower limit, compared with 1.038 K at 1 Pa. Both pass nominally, but their margins differ substantially. At 100,000 Pa, residence is only 0.277 s despite entry at 2.362 s. The zero-gas row is a limiting calculation, not a confirmed fabrication condition.

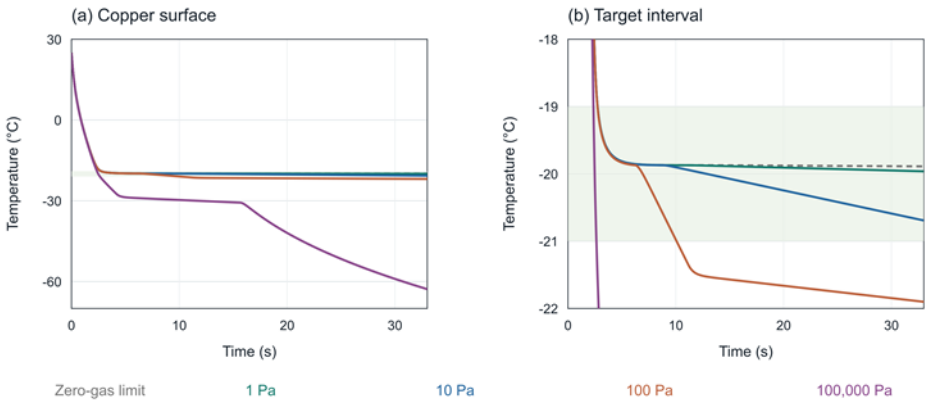


Figure 3: Copper temperature response

Unloading and heat leakage

The nominal initial force of 63.000 mN falls to 1.224 mN at entry, a reduction of about 98%. Release occurs at −19.872 °C. Figure 4 therefore links rapid initial cooling to unloading within the target band, but zero force does not imply zero heat transfer. A kinematic interference interval of 34.32–35.88 μm places release within the band without guaranteeing sufficient thermal isolation.

Table 4: Dominant assumption sensitivities

Zero-gas change	Entry, s	Residence, s	3 s/30 s
Reference	2.746	≥30.253	Pass
h* × 0.25	4.323	≥28.676	Fail
$G_b = 10^{-4}$ W/K	2.737	≥30.263	Pass
$G_b = 10^{-3}$ W/K	2.651	7.382	Fail
$Q_{ph} = 0$	2.746	≥30.253	Pass

Table 4 isolates changes at nominal geometry in the zero-gas limit. Reducing h* fourfold delays entry to 4.323 s, violating the entry criterion. A bypass of 10^{-4} W/K retains nominal compliance, whereas 10^{-3} W/K shortens residence to 7.382 s. Setting Q_{ph} to zero leaves the response unchanged while preserving sensible capacity. The bulk remains above the assumed freezing interval in this control, so thermal isolation and sensible storage account for residence; latent-storage benefit is not demonstrated.

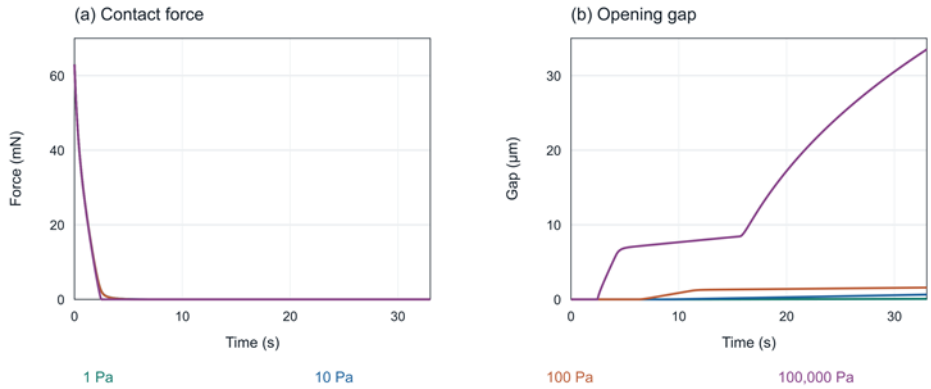


Figure 4: Contact force and separation

Nominal feasibility and tested tolerance corners

The joint criteria leave a narrow overlap between sufficient loading and adequate isolation. Figure 5 locates these competing exclusions; Table 5 tests whether nominal passes retain that overlap under geometric deviations. Figure 5 uses L_a = 2.00 mm, t_b = 0.100 mm and $\kappa_s = 39 \times 10^{-6}$ K^{-1}; each cell is a sampled result, not a certified continuous region.

Table 5: Nominal and tolerance feasibility

p_g, Pa	Grid size	Passes	Corners tested	All-corner passes
1	3600	148	2368	0
10	3600	68	1088	0
100	3600	0	0	0

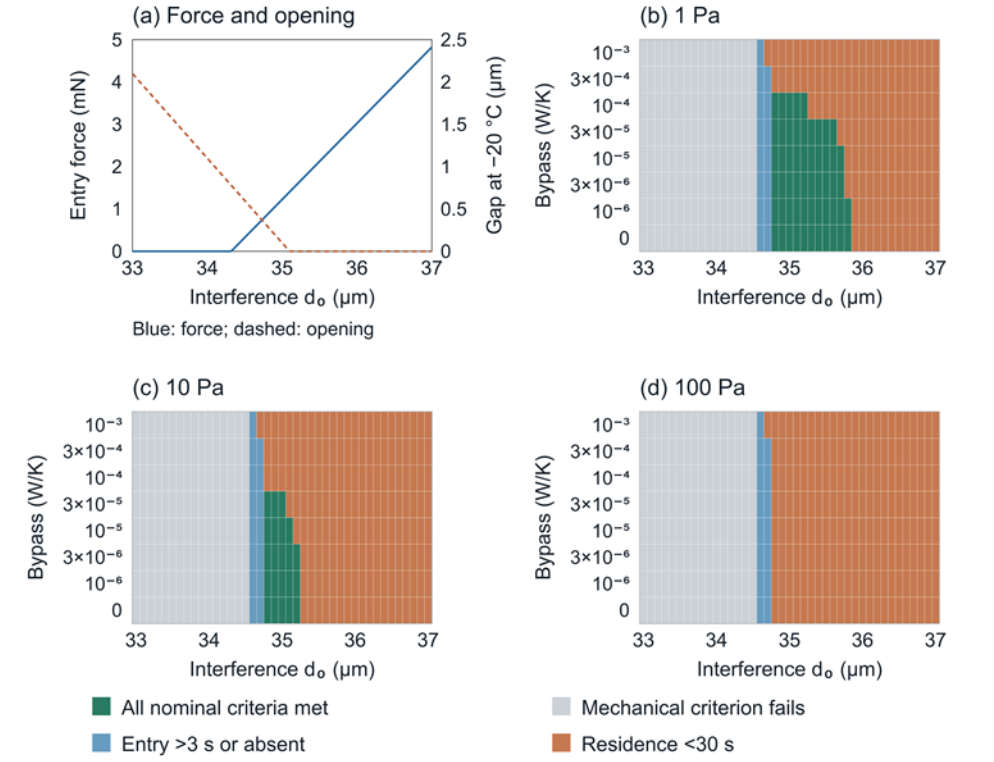


Figure 5: Gap force and leakage feasibility

At 1 and 10 Pa, 148/3600 (4.11%) and 68/3600 (1.89%) sampled points pass, respectively; none passes at 100 Pa. No nominally feasible candidate passed all 16 tested tolerance corners. Each of the 216 candidates has at least one failing corner among 3456 evaluated cases. The independent audit also identifies a mechanical-failure corner for every candidate, so rejection of this fixed candidate set does not rely on time-step resolution of thermal crossings. This does not mean that every interior tolerance point fails or that no other nominal design exists. Figure 5 holds arm geometry fixed: low interference violates loading, while stronger coupling can sustain excessive cooling; bypass leakage further restricts the overlap. The nominal candidate set remains conditional on R_s = 22.80 K W^{-1}, g_r = 1 µm and the stated mechanical gates.

Resistance and near-contact sensitivity

The reference-network exclusion is meaningful only if it is distinguished from sensitivity to unknown resistance and near-contact closure. Table 6 varies one of these inputs at a time at nominal geometry.

Table 6: Resistance and regularization effects

Varied input	p_g, Pa	Entry, s	Residence, s
R_s = 1 K/W	1	0.880	≥32.119
R_s = 22.80 K/W	1	2.746	≥30.253
R_s = 30 K/W	1	3.542	≥29.458
R_s = 45 K/W	1	5.289	≥27.710
g_r = 0.1 μm	100	2.738	7.313
g_r = 1 μm	100	2.738	7.333
g_r = 5 μm	100	2.738	7.425
g_r = 0.1 μm	100,000	2.248	0.203
g_r = 1 μm	100,000	2.362	0.277
g_r = 5 μm	100,000	2.527	0.736

Increasing R_s from 22.80 to 30 K/W delays entry from 2.746 to 3.542 s, crossing the 3 s limit although no exit is observed by 33 s. Greater resistance can improve isolation while obstructing initial cooling. At 1 K/W, entry is 0.880 s. These nominal trends neither establish tolerance compliance at another resistance nor uniquely identify boundary, mounting and spreading contributions.

The additional nominal sensitivity at 1 Pa gives entry times of 2.508, 2.992 and 3.372 s at 0.90, 1.10 and 1.25 times the reference R_s, respectively. The +10% case passes with only 0.0077 s remaining to the entry limit, whereas the +25% case fails. These are model margins, not experimental accuracy estimates. At 100 Pa, none of the tested resistance factors from 0.5 to 2 restores 30 s residence. The 148/68/0 grid counts have not been recomputed at these alternative resistances.

At 100 Pa, changing g_r from 0.1 to 5 μm increases residence from 7.313 to 7.425 s; at 100,000 Pa it increases from 0.203 to 0.736 s. The stronger high-pressure dependence follows from reduced dominance of the jump length ζλ. Neither case approaches 30 s. At 1–10 Pa, all three g_r values retain censored residence above 30 s, while the zero-gas result is independent of g_r. This 15-case sensitivity tests the closure at nominal geometry; it does not repeat the full search or validate near-contact physics.

An additional 81-case nominal scenario study examines resistance, stiffness, contact, gas properties and phase excess. At 1 Pa, halving k0 delays entry to 3.327 s; doubling it shortens entry to 2.414 s but produces 126 mN initial force, exceeding the provisional 100 mN gate. At 10 Pa, the gas-property alternatives give observed residence from 16.375 s to censored lower bounds above 30 s, so nominal compliance at 10 Pa is not insensitive to the assumed gas properties. At 100 Pa, all nine gas-property alternatives

remain below 30 s. Scaling Qph from zero to 1.5 times its reference leaves entry and first residence numerically unchanged at the three reference pressures; that finding concerns this operating interval and fixed sensible inventory.

Discussion

Nominal feasibility does not ensure compliance at the tested tolerance corners. Contact must initially conduct strongly enough to meet the 3 s entry limit, yet unloading must suppress heat loss enough to sustain 30 s in the band. Length and thickness change both retraction and stiffness, while interference controls release. Their coupled effects explain why free stroke or contact force alone cannot define feasibility. The 16-corner test is a discrete stress test of each sampled candidate, not an exhaustive classification of the continuous tolerance domain.

At low pressure, the jump length dominates gas transfer, so changing an already small separation has little effect. Near continuum conditions, g_r and gap size influence heat leakage more strongly. The approximately 0.013 μm nominal zero-gas separation is not a confirmed manufacturing clearance. Residual solid bridges and unresolved surface geometry prevent interpreting weak g_r sensitivity as validation of the near-contact law.

The resistance inventory is equally consequential: 98.97% of the reference R_s is not explained by the two illustrative metal sections. The lack of all-corner passes therefore applies to the reference network, not every boundary condition. Likewise, the unchanged zero-phase-excess control demonstrates isolation-dominated residence in that scenario; it does not establish that PCM is generally ineffective.

Physical validation requires measured force–displacement and contact/gap conductance, pressure history and capsule-scale cooling enthalpy, followed by independent surface-temperature measurements with uncertainty quantified (Joint Committee for Guides in Metrology, 2008). The strip model neglects formed-arm coupling and the supplier’s stated linear range begins at −20 °C; colder actuator predictions are extrapolations. A spatial model and experiments remain necessary to test uniformity and strength, but are not presented here as completed results.

Unverified U6: the isothermal copper face, Ta = Tc, fixed bath temperature, massless junction and omitted thermal paths require assembly-specific checks. Supplier or literature support for an individual property does not validate those reductions. The U1–U6 statements in this manuscript identify the unresolved physical inputs.

Conclusions

The reference model gives 148, 68 and 0 nominal passes at 1, 10 and 100 Pa. None of the 216 candidates passes all 16 tolerance corners, and each has an independently verified mechanical-failure corner. This excludes the tested candidate set under the stated gates; it does not establish nonexistence of a feasible continuous design. Resistance, gas-property and stiffness scenarios can change nominal compliance, so the counts are conditional predictions. The unassigned 98.97% of the reference external resistance and the unverified contact and capsule-scale PCM behavior prevent physical qualification. The accompanying grid dataset documents the nominal search; experimental identification of the assembly remains necessary.

Conflict of Interest: The author reported no conflict of interest.

Data availability: The accompanying junction_grid.csv contains all 10,800 nominal configuration records. Appendix A of the accompanying response letter describes the parameter grid, numerical procedure and CSV conventions. The submission comprises this manuscript, the response letter and junction_grid.csv. No source-code archive, separate supplementary document or corner-level dataset accompanies this submission.

Funding Statement: The author did not obtain any funding for this research.

References:

1. Aperam Alloys Imphy. (2025, May). *Thermostatic bimetal high flexivity SP series* [Data sheet]. https://www.aperam.com/sites/default/files/documents/BIMETAL%20High%20Flexivity%20EN%20MAY%202025%20EN.pdf
2. Bianco, V., De Rosa, M., and Vafai, K. (2022). Phase-change materials for thermal management of electronic devices. *Applied Thermal Engineering, 214*, Article 118839. https://doi.org/10.1016/j.applthermaleng.2022.118839
3. Castelli, L., Garg, A., Zhu, Q., Sashital, P., Shimokusu, T. J., and Wehmeyer, G. (2023). A thermal regulator using passive all-magnetic actuation. *Cell Reports Physical Science, 4*, Article 101556. https://doi.org/10.1016/j.xcrp.2023.101556
4. COMSOL AB. (n.d.). *Theory for thermal contact* (COMSOL Multiphysics 6.4 Heat Transfer Module documentation). Retrieved October 26, 2026, from https://doc.comsol.com/6.4/doc/com.comsol.help.heat/heat_ug_theory.07.094.html

5. Cooper, M. G., Mikic, B. B., and Yovanovich, M. M. (1969). Thermal contact conductance. *International Journal of Heat and Mass Transfer, 12*, 279–300. https://doi.org/10.1016/0017-9310(69)90011-8
6. Farid, M. M., Khudhair, A. M., Razack, S. A. K., and Al-Hallaj, S. (2004). A review on phase change energy storage: materials and applications. *Energy Conversion and Management, 45*, 1597–1615. https://doi.org/10.1016/j.enconman.2003.09.015
7. Guo, L., Zhang, X., Huang, Y., Hu, R., and Liu, C. (2017). Thermal characterization of a new differential thermal expansion heat switch for space optical remote sensor. *Applied Thermal Engineering, 113*, 1242–1249. https://doi.org/10.1016/j.applthermaleng.2016.11.102
8. Heinz, A., and Moser, C. (2023). Numerical modelling and experimental testing of a thermal storage system with non-spherical macro-encapsulated phase change material modules. *Journal of Energy Storage, 58*, Article 106427. https://doi.org/10.1016/j.est.2022.106427
9. Joint Committee for Guides in Metrology. (2008). *Evaluation of measurement data—Guide to the expression of uncertainty in measurement* (JCGM 100:2008). https://doi.org/10.59161/JCGM100-2008E
10. Kommandur, S., and Kishore, R. A. (2023). Contact-based passive thermal switch with a high rectification ratio. *ACS Engineering Au, 3*, 76–83. https://doi.org/10.1021/acsengineeringau.2c00046
11. Park, S. W., Li, J., and Weisensee, P. B. (2024). Development of a fully packaged passive thermal regulator. *Scientific Reports, 14*, Article 16979. https://doi.org/10.1038/s41598-024-67758-4
12. Righetti, G., Zilio, C., Doretti, L., Longo, G. A., and Mancin, S. (2021). On the design of phase change materials based thermal management systems for electronics cooling. *Applied Thermal Engineering, 196*, Article 117276. https://doi.org/10.1016/j.applthermaleng.2021.117276
13. Rubitherm Technologies GmbH. (2022, July 12). *SP-21 technical data sheet* [Data sheet]. https://www.rubitherm.com/media/products/datasheets/Techdata_-SP-21_EN_12072022.PDF
14. Shivalik Bimetal Controls. (n.d.). *Thermostatic bimetal handbook*. https://www.shivalikbimetals.com/Catalogue.pdf
15. Specialty Coating Systems. (2022, March 2). *A guide to Parylene service temperatures*. https://scscoatings.com/newsroom/blog/a-guide-to-parylene-service-temperatures/

16. Tan, B., Lyu, J., Yang, F., Xu, K., Qiao, S., Song, B., Yang, L., and Liu, K. (2026). Bistable origami thermal switch with high switching ratios. *Nature Communications, 17*, Article 3177. https://doi.org/10.1038/s41467-026-69956-2
17. Timoshenko, S. (1925). Analysis of bi-metal thermostats. *Journal of the Optical Society of America, 11*(3), 233–255. https://doi.org/10.1364/JOSA.11.000233
18. Voller, V. R., Cross, M., and Markatos, N. C. (1987). An enthalpy method for convection/diffusion phase change. *International Journal for Numerical Methods in Engineering, 24*, 271–284. https://doi.org/10.1002/nme.1620240119
19. Voller, V. R., and Prakash, C. (1987). A fixed grid numerical modelling methodology for convection-diffusion mushy region phase-change problems. *International Journal of Heat and Mass Transfer, 30*(8), 1709–1719. https://doi.org/10.1016/0017-9310(87)90317-6
20. Xiao, Z., Kishore, R., and Booten, C. (2025). Demonstration and characterization of insertable passive thermal switches for dynamic building envelopes. *Cell Reports Physical Science, 6*, Article 102668. https://doi.org/10.1016/j.xcrp.2025.102668
21. Zalba, B., Marín, J. M., Cabeza, L. F., and Mehling, H. (2003). Review on thermal energy storage with phase change: materials, heat transfer analysis and applications. *Applied Thermal Engineering, 23*, 251–283. https://doi.org/10.1016/S1359-4311(02)00192-8